Reversible Redox Chemistry in Pyrrolidinium-Based TEMPO Radical and Extended Viologen for High-Voltage and Long-Life Aqueous Redox Flow Batteries

*Mingguang Pan, Liuzhou Gao, Junchuan Liang, Pengbo Zhang, Shuyu Lu, Yan Lu, Jing Ma, and Zhong Jin**

Aqueous organic redox flow batteries (AORFBs) are regarded as a promising candidate for grid-scale, low-cost and sustainable energy storage. However, their performance is restricted by low aqueous solubility and the narrow potential gap of the organic redox-active species. Herein, a highly-soluble organic redox pair based on pyrrolidinium cation functionalized TEMPO and extended viologen, namely Pyr-TEMPO and [PyrPV]Cl_4, which exhibits high cell voltage (1.57 V) and long cycling life (over 1000 cycles) in AORFBs is reported. The intrinsic hydrophilic nature of the pyrrolidinium group enables high aqueous solubilities (over 3.35 м for Pyr-TEMPO and 1.13 м for [PyrPV]Cl_4). Furthermore, the interaction of nitroxyl radicals with water is observed, which may be helpful to prevent collision-induced side reactions or structure decomposition. Notably, the assembled AORFBs realize a high energy density of 16.8 Wh L^{-1} and a peak power density of 317 mW cm^{-2}. The evidence is provided to clarify the capacity degradation mechanism of TEMPO/viologen AORFB systems by a series of comprehensive characterizations. Furthermore, the reversible consumption and re-generation of the nitroxyl radicals upon charging and discharging are well understood. This work presents effective electrochemical and spectroscopic approaches to clarify the redox chemistry and capacity degradation mechanism of radical incorporating AORFB systems.

1. Introduction

Renewable energy sources, such as solar and wind power, show considerable promise in reducing carbon footprints and addressing the world-wide environment crisis.[1] However, their intermittent and fluctuating nature calls for affordable and sustainable energy-storage technologies at grid scales (MW/MWh). The ingenious configuration of redox flow batteries (RFBs) with favorable scalability, reliable safety, and excellent stability can provide a good choice to meet this demand.[2–5] However, the extensively studied all-vanadium RFBs suffer some long-standing problems, such as the high costs of cation exchange membranes and vanadium-based active materials and the electrolyte crossover and corrosion issues in strong acidic conditions.[6] Aqueous organic redox flow batteries (AORFBs), after being reported,[7,8] received particular attention among the existing flow battery technologies, primarily because organic redox-active materials possess numerous advantages including great natural abundance, facile structural tailorability, tunable electrochemical properties, and potentially low costs. The solutions of a number of organic active molecules, such as viologen, anthraquinone, phenazine, and azobenzene derivatives, have been investigated as the anolytes for AORFBs.[9–32] And a few organic molecules are available for the catholytes, typically, 2,2,6,6-tetramethyl piperidin-1-yl)oxyl (TEMPO) and metallocene derivatives.[17–32] Considering the high redox potential of TEMPO and its derivatives (ranged from 0.8 to 1.0 V versus standard hydrogen electrode, SHE), the introduction of highly hydrophilic groups, such as the quaternary ammonium group, is a promising approach to further improve the energy density.[20,23] However, up to date, the capacity degradation mechanism on the TEMPO/viologen systems remains unclear, and a lack of appropriate spectroscopic methods was established to study the electrochemical reversibility of redox-active organic species, especially in radical involved systems.

Given that the chemically stable pyrrolidinium group has an ultrawide electrochemical window and strong polarity, it has been frequently utilized as a cationic moiety of ionic liquids.[33,34] When coupled with Cl^- ion, the pyrrolidinium functionalized organic species also appear to be highly water-soluble. Herein, we report the successful synthesis of pyrrolidinium cation functionalized TEMPO and extended viologen (Pyr-TEMPO and [PyrPV]Cl_4), which can serve as a highly-soluble organic redox pair with high cell voltage and excellent redox reversibility in AORFBs (**Figure 1**). The introduction

M. Pan, L. Gao, J. Liang, P. Zhang, S. Lu, Y. Lu, J. Ma, Z. Jin
Key Laboratory of Mesoscopic Chemistry of MOE
Jiangsu Key Laboratory of Advanced Organic Materials
School of Chemistry and Chemical Engineering
Nanjing University
Nanjing 210023, China
E-mail: zhongjin@nju.edu.cn

The ORCID identification number(s) for the author(s) of this article can be found under https://doi.org/10.1002/aenm.202103478.

DOI: 10.1002/aenm.202103478

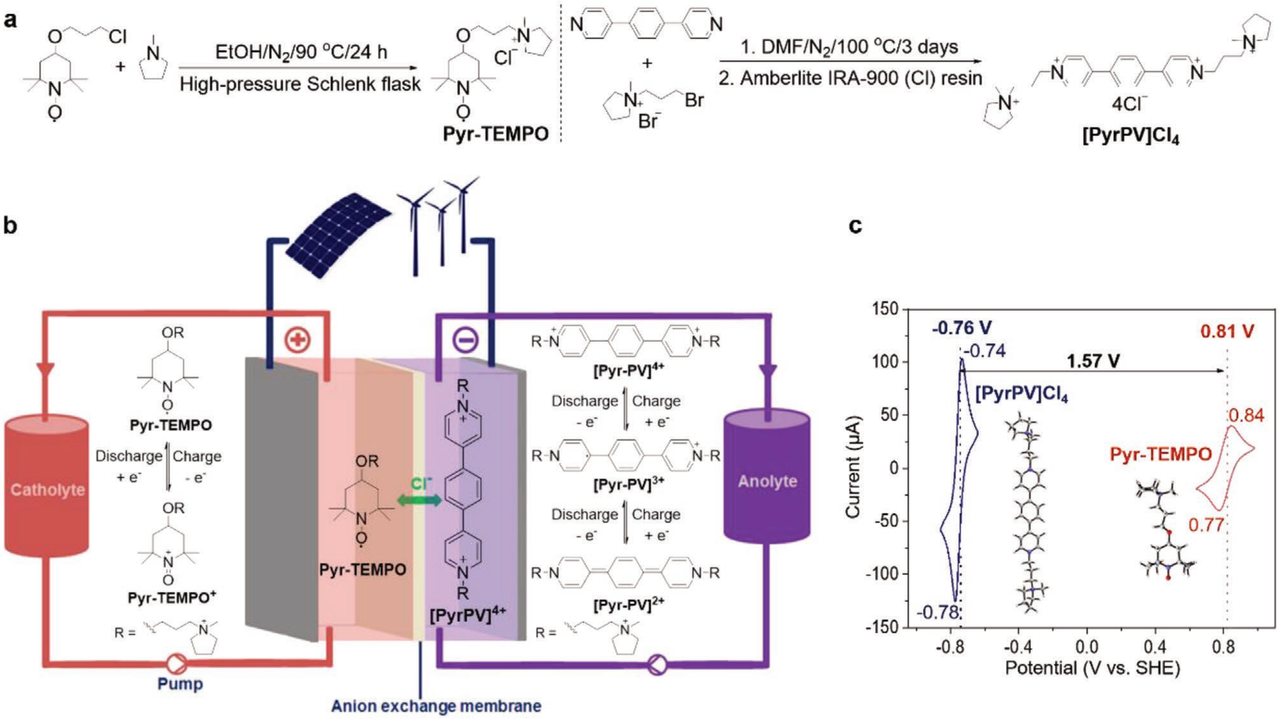

Figure 1. Synthesis processes and working mechanism of pyrrolidinium functionalized TEMPO and extended viologen. a) Synthetic routes of Pyr-TEMPO and [PyrPV]Cl$_4$. b) Structural configuration and the cathodic/anodic redox processes of Pyr-TEMPO/[PyrPV]Cl$_4$ AORFBs. c) CV curves of 4.0 mM [PyrPV]Cl$_4$ and Pyr-TEMPO dissolved in 0.5 м NaCl solutions, respectively.

of the hydrophilic pyrrolidinium group brought ultrahigh aqueous solubilities (more than 3.35 м for Pyr-TEMPO and 1.13 м for [PyrPV]Cl$_4$). Moreover, the interaction between nitroxyl radicals and water molecules, was verified by the no-deuterium nuclear magnetic resonance (No-D NMR) and electron paramagnetic resonance (EPR) spectroscopic studies, maybe helping to prevent the collision-caused side reactions of nitroxyl radicals and thus improving the cycling performance. In addition, the introduction of grafted pyrrolidinium terminals has no obvious influence on the redox potential, thus guaranteeing a high cell voltage (1.57 V) of the Pyr-TEMPO/[PyrPV]Cl$_4$ AORFBs. As a result, the Pyr-TEMPO/[PyrPV]Cl$_4$ AORFBs demonstrated an excellent Coulombic efficiency of nearly 100%, a high energy efficiency of 84%, and an ultralow capacity fade rate of 0.05% per cycle for over 1000 cycles at high electrolyte concentrations. The assembled AORFBs realized an energy density of 16.8 Wh L^{-1} and a peak power density of 317 mW cm^{-2}, which are competitive among the state-of-the-art pH-neutral AORFBs (Table S1, Supporting Information).[23–28] Furthermore, the capacity degradation mechanism of Pyr-TEMPO/[PyrPV]Cl$_4$ AORFBs was comprehensively clarified by the ^{1}H NMR and high-resolution electrospray ionization mass spectrometry (HRESIMS). All the spectroscopic data revealed that the decomposition and crossover of TEMPO species, rather than viologen species, should be the main causes for capacity degradation. Moreover, the excellent electrochemical reversibility of Pyr-TEMPO accompanied with the reversible consumption/re-generation of radicals was verified by the No-D NMR technique during the cycling process.

2. Results and Discussions

The synthesis approaches of Pyr-TEMPO and [PyrPV]Cl$_4$ are shown in Figure 1a. Briefly, Pyr-TEMPO was synthesized through a reaction of 4-(2,2,6,6-tetramethyl-1-oxyl-4-piperidoxyl) propyl chloride and 1-methylpyrrolidine at the molar of 2:1 in a sealed flask under N$_2$ atmosphere at 90 °C for 24 h, with a yield of 76.7%. [PyrPV]Cl$_4$ was prepared via the N-alkylation reaction of 4,4'-(1,4-phenylene)bispyridine and 1-(3-bromopropyl)-1-methylpyrrolidin-1-ium bromide, followed by the anion exchange of Br$^-$ to Cl$^-$ using an Amberlite IRA-900 (Cl) resin column, with an overall yield of 92.0%. The NMR spectra of the as-prepared samples are presented in Figure S1–S3, Supporting Information, confirming the successful synthesis of these two redox-active materials with high purity. Moreover, Pyr-TEMPO displayed ultrahigh solubilities in deionized water (>3.35 м) and 2.0 м NaCl solution (>2.84 м), respectively, attributing to pyrrolidinium functionalization (Figure S4, Supporting Information). On the other hand, [PyrPV]Cl$_4$ also exhibited high solubilities in deionized water (1.13 м) and 2.0 M NaCl solution (1.08 м), respectively (Figure S5, Supporting Information).

Through density functional theory (DFT) simulation, the optimized structures and calculated energy levels of Pyr-TEMPO and [PyrPV]Cl$_4$ at different redox states were studied, as presented in Figure S6a,b, Supporting Information, respectively, suggesting the single-electron redox process of Pyr-TEMPO and two single-electron redox processes of [PyrPV]Cl$_4$. At the pristine state, the Mulliken charges of N and O in the redox center of Pyr-TEMPO were calculated to be 0.087 and –0.313, respectively; after losing an electron, these two values turned to be 0.249 and –0.026 (Figure S6a, Supporting Information). After accepting one electron, the spin density of monoradical $[PyrPV]^{3+}$ (SOMO-α and SOMO-β) was delocalized and stabilized on the 1,4-di(pyridin-4-yl)benzeneskeleton, and after accepting another electron, a closed-shell quinoid was generated (Figure S6b, Supporting Information). The potential gap between Pyr-TEMPO and $[PyrPV]Cl_4$ was predicted to be approximately 1.73–1.77 V by using the DFT methods, which matched well with the experimental value of 1.57 V (Table S2, Supporting Information, and Figure 1c).[35,36] Benefitting from the large gap (1.57 V) of their redox potentials together with high aqueous solubilities, the as-obtained Pyr-TEMPO and $[PyrPV]Cl_4$ molecules were envisioned to serve as promising cathodic and anodic active materials in high-voltage pH-neutral AORFBs, respectively (Figure 1b,c). The CV analyses of 4.0 mM Pyr-TEMPO in 0.5 м NaCl solution exhibited a reduction potential at 0.77 V and an oxidation potential at 0.84 V versus SHE (Figure 1c). In contrast, the CV curve of 4.0 mM $[PyrPV]Cl_4$ electrolyte showed a formal potential (the average value of the anodic peak and cathodic peak potentials) of –0.76 V versus SHE. Notably, the CV of $[PyrPV]Cl_4$ displayed one broad reversible redox couple derived from the two single-electron reductions of the initial cationic form to the monoradical form and then to the quinoid form.

Interestingly, it is a controversial question that whether a two-electron or two single-electron redox possesses proceed for phenylene bridging bipyridinium derivatives.[37,38] Herein, we propose a simple and effective method to clarify this question. As revealed by the CV curves in Figure S7a, Supporting Information, the one broad redox couple of $[PyrPV]Cl_4$ was gradually split into two overlapped couples when increasing the concentration of $[PyrPV]Cl_4$ from 2 to 100 mM in a 2 м NaCl aqueous solution, unambiguously confirming the two single-electron reductions. Moreover, the differential pulse voltammetry (DPV) curves of $[PyrPV]Cl_4$ (Figure S7b, Supporting Information) showed that a reduction peak was gradually split into two peaks when the concentration increased, further verifying the two single-electron reductions of phenylene bridging bipyridinium systems.

The electrochemical properties of Pyr-TEMPO and $[PyrPV]Cl_4$ were investigated. The CV profiles of Pyr-TEMPO at scan rates from 20 to 100 mV s^{-1} showed a reversible redox couple at +0.81 V versus SHE (Figure S8a, Supporting Information). Both the oxidation and reduction peak currents had a linear relationship with the square root of the scan rate ($\nu^{1/2}$), indicating a reversible and diffusion-controlled redox process of Pyr-TEMPO (Figure S8b, Supporting Information). Moreover, the CV curves of Pyr-TEMPO revealed an outstanding redox reversibility during 1000 cycles (Figure S9, Supporting Information). The electrochemical kinetics properties of Pyr-TEMPO, including the diffusion coefficient (D) and kinetic rate constant (k_0), were studied by using linear sweep voltammetry (LSV) on a glassy carbon rotating disk electrode (Figure S8c–f, Supporting Information). The LSV scans of Pyr-TEMPO were conducted at a rate of 5 mV s^{-1} from 0.40 to 1.20 V versus SHE (Figure S8c, Supporting Information). The linear Levich plot was constructed for the single-electron reduction of Pyr-TEMPO using the limiting current (i) and the square root of the rotation speed ($\omega^{1/2}$), where the D value was obtained as $(4.07 \pm 0.08) \times 10^{-6}$ cm^2 s^{-1} after background current calibration (Figure S8d, Supporting Information). According to the Koutecký-Levich equation and Tafel plot (Figure S8e,f, Supporting Information), the rate constant (k_0) and charge transfer coefficient (α) of Pyr-TEMPO were calculated as $(1.42 \pm 0.07) \times 10^{-2}$ cm s^{-1} and 0.53 ± 0.02, respectively, indicating the fast electron transfer kinetics.[10,15,18,39] Notably, the CV profiles of 4 mM $[PyrPV]Cl_4$ in a 0.5 м NaCl aqueous solution displayed one broad reversible redox couple at –0.76 V versus SHE (Figure 1c and Figure S10, Supporting Information), attributing to the completely overlapped two single-electron reductions. The D, k_0, and α values of $[PyrPV]Cl_4$ were calculated as $(2.27 \pm 0.10) \times 10^{-6}$ cm^2 s^{-1}, $(5.94 \pm 0.55) \times 10^{-3}$ cm s^{-1} and 0.61 ± 0.03, respectively (Figure S10c–f, Supporting Information). The D and k_0 values of Pyr-TEMPO and $[PyrPV]Cl_4$ are very competitive among organic redox-active species.[18] Furthermore, the k_0 values were also calculated by the Nicholson method (Figure S11 and S12, Supporting Information) and compared in Table S3, Supporting Information. The difference of k_0 values calculated by the Koutecký-Levich method and the Nicholson method (Table S3, Supporting Information) has already been noticed in the previous literature.[13,17]

A typical flow battery was constructed by using 0.2 м Pyr-TEMPO and 0.1 м $[PyrPV]Cl_4$ dissolved in 2.0 м NaCl solutions as catholyte and anolyte respectively, and a Selemion DSV anion-exchange membrane was used as the separator for Cl^- exchange (Figure 1b and **Figure 2**). To guarantee the complete redox reaction of the Pyr-TEMPO catholyte and avoid anolyte-derived capacity loss, excess $[PyrPV]Cl_4$ anolyte was used in the AORFB, thus allowing the durable cycling of Pyr-TEMPO. As revealed in Figure 2a, the Pyr-TEMPO/$[PyrPV]Cl_4$ AORFBs demonstrated exceptionally high charge and discharge voltages compared to other flow battery systems. During the 500 cycles (≈105.4 h), the Coulombic efficiency was stabilized as high as ≈100%, confirming the excellent redox reversibility and stability of Pyr-TEMPO. In the first discharge step, the AORFB with 0.2 м Pyr-TEMPO anolyte delivered a capacity of 4.64 Ah L^{-1}, which was 87% of the theoretical capacity limit for single-electron storage (5.36 Ah L^{-1}). In the initial 10 cycles, the discharge capacity gradually increased, probably due to the activation of anion-exchange membrane, and then stabilized at ≈4.8 Ah L^{-1} for the next 60 cycles. Moreover, the charge and discharge voltage plateaus of the AORFB at the current density of 40 mA cm^{-2} were well maintained at 1.61 and 1.38 V, respectively, demonstrating the high operation voltage and favorable electrochemical stability (Figure 2b,c). Moreover, the AORFB exhibited outstanding rate capability at current densities ranging from 40 to 100 mA cm^{-2} (Figure 2d,e). For instance, the discharge capacity at 100 mA cm^{-2} is 4.36 Ah L^{-1}, providing a ≈92.4% capacity retention relative to the value at 40 mA cm^{-2} (4.72 Ah L^{-1}). As shown in **Figure 3**g, the Pyr-TEMPO/$[PyrPV]Cl_4$ AORFBs maintained a Coulombic efficiency of ≈100%, an ultrahigh energy efficiency of ≈85% and a remarkable total capacity retention of 79.7% after 500 cycles (corresponding to a capacity fade rate of 0.04% per cycle or 4.56% per day). With 1.0 м Pyr-TEMPO catholyte and 0.5 м $[PyrPV]Cl_4$ anolyte, the AORFB delivered an initial volumetric capacity as high as 23.9 Ah L^{-1}, accompanied by a Coulombic efficiency of ≈100%,

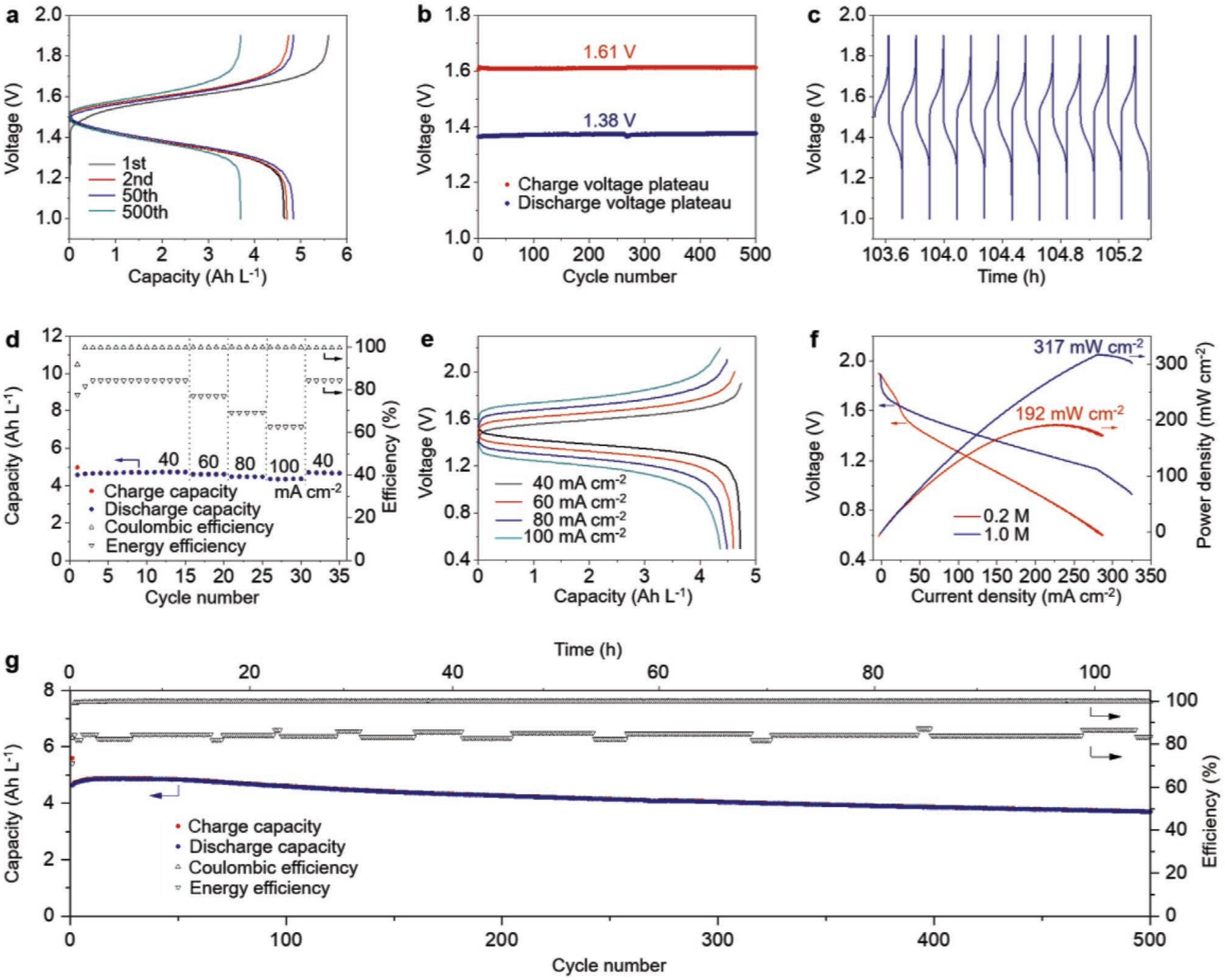

Figure 2. Battery performances of the Pyr-TEMPO/[PyrPV]Cl_4 AORFB. a) Typical galvanostatic charge-discharge profiles. b) Charge and discharge voltage plateaus per cycle during 500 charge-discharge cycles. c) Representative voltage versus time curves were recorded between the 491st and 500th cycles. d) Rate capability test between 40 to 100 mA cm^{-2}, showing the charge capacity, discharge capacity, Coulombic efficiency, and energy efficiency versus the cycle number. e) Representative charge-discharge curves at different current densities. f) *I–V* polarization and power density of Pyr-TEMPO/[PyrPV]Cl_4 AORFBs with different Pyr-TEMPO concentrations (0.2 M and 1.0 M) at ≈100% state of charge. g) Cycling performance, showing the charge capacity, discharge capacity, Coulombic efficiency, and energy efficiency versus the cycle number. Conditions (unless stated otherwise): catholyte, 0.2 M Pyr-TEMPO in 2.0 M NaCl; anolyte, 0.1 M [PyrPV]Cl_4 in 2.0 M NaCl; current density, 40 mA cm^{-2}; separator, DSV anion-exchange membrane; room temperature.

an energy efficiency of 84%, and a capacity fade rate of 0.2% per cycle for over 250 cycles (corresponding to a time-dependent decay rate of 5.73% per day) (Figure S13, Supporting Information). Furthermore, the AORFB with 1.0 M Pyr-TEMPO/0.5 M [PyrPV]Cl_4 at ≈100% state of charge reaches a maximum power density of 317 mW cm^{-2} with a corresponding current density of 280 mA cm^{-2} (Figure 2f), which is among the highest records in pH-neutral AORFBs (Table S1, Supporting Information).[18–23]

The long-term cycling performances of AORFB with the electrolyte concentrations of 0.5 M Pyr-TEMPO and 0.25 M [PyrPV]Cl_4 were also investigated (Figure 3a and Table S4, Supporting Information). The AORFB delivered a high capacity of 10.86 Ah L^{-1} and a low capacity fade rate of 0.05% per cycle for over 1000 cycles (a time-dependent decay rate of 3.47% per day), as well as high Coulombic efficiency (≈100%) and energy efficiency (≈84%). To clarify the capacity degradation mechanism during long-term cycling processes, the ^{1}H NMR and high-resolution electrospray ionization mass spectrometry (HRESIMS) studies were performed. As revealed by the ^{1}H NMR spectra (Figure 3b,c), the decomposition and crossover of Pyr-TEMPO should be primarily responsible for the capacity degradation. Specifically, the new NMR peaks that emerged in Pyr-TEMPO catholyte after galvanostatic cycling (marked as "✻" in Figure 3b) indicate the decomposition of Pyr-TEMPO was probably due to the cleavage of nitroxyl radicals from N–O• to N–H, as indicated by the HRESIMS analysis (Figure S14, Supporting Information). On the other hand, the observed new NMR peaks in [PyrPV]Cl_4 anolyte after cycling (marked as "◇" and "Δ" in Figure 3c) were originated from the crossover of Pyr-TEMPO. Normally, owing to the shielding effect of nitroxyl

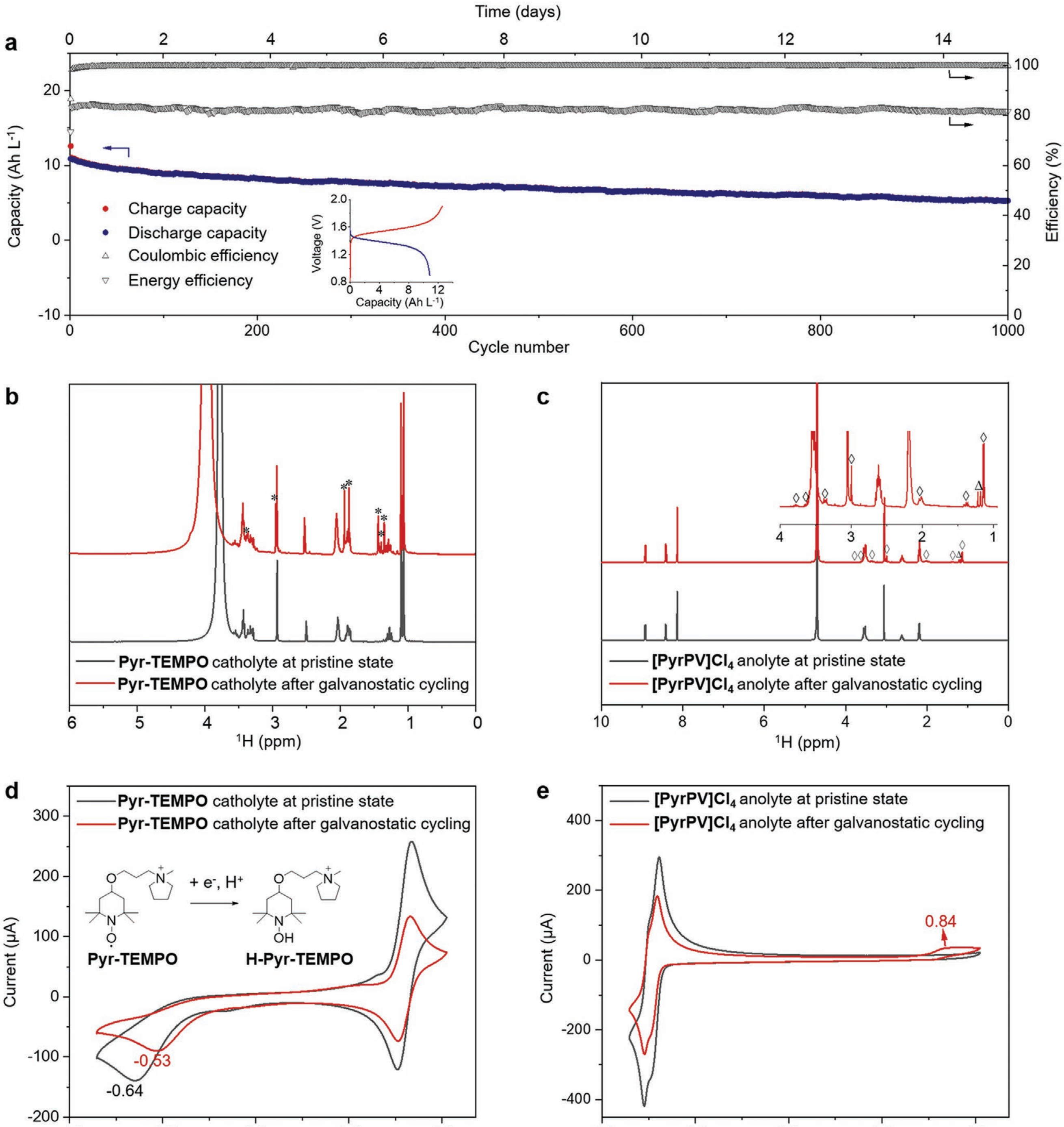

Figure 3. Long-term cycling performances and capacity degradation mechanism studies. a) Cycling performances of the Pyr-TEMPO/[PyrPV]Cl$_4$ AORFB, showing the charge capacity, discharge capacity, Coulombic efficiency, and energy efficiency versus the cycle number. The inset shows the charge and discharge curves in the first cycle. Conditions: catholyte, 0.5 м Pyr-TEMPO in 2.0 м NaCl; anolyte, 0.25 м [PyrPV]Cl$_4$ in 2.0 м NaCl; current density, 40 mA cm^{-2}; separator, DSV anion-exchange membrane; room temperature. b) ^{1}H NMR spectra (DMSO-d_6) of Pyr-TEMPO at the pristine state and after galvanostatic cycling, respectively. Herein, the Pyr-TEMPO samples were reduced by phenyl hydrazine prior to the NMR tests. The peaks marked with "*" represent the impurities derived from the decomposition of Pyr-TEMPO. c) ^{1}H NMR spectra (D_2O) of [PyrPV]Cl$_4$ at the pristine state and after galvanostatic cycling, respectively. The peaks marked with "◊" and "Δ" are derived from the hydrogenated Pyr-TEMPO (H-Pyr-TEMPO) and other decomposition products, respectively. The inset shows the magnified NMR spectrum after galvanostatic cycling in the range of 1–4 ppm. d) and e) CV curves of Pyr-TEMPO and [PyrPV]Cl$_4$ at the pristine state and after galvanostatic cycling, respectively. The solutions for CV tests were prepared by diluting 200 µl of the corresponding electrolyte with 4 ml 2.0 м NaCl aqueous solutions. The inset in (d) illustrates the irreversible hydrogenation of Pyr-TEMPO to H-Pyr-TEMPO.

radicals, the NMR peaks of Pyr-TEMPO should be broadened, or even hard to observe. In this case, the peaks (marked as "◊" in Figure 3c) should be assigned to the irreversibly hydrogenated Pyr-TEMPO (H-Pyr-TEMPO), because these peaks are almost identical to those of Pyr-TEMPO treated by phenylhydrazine. Once a Pyr-TEMPO molecule crossed into [PyrPV]Cl_4 anolyte, it accepted an electron and a proton during the discharging process, thus resulting in the formation of H-Pyr-TEMPO, which was further verified by the HRESIMS analysis (Figure S15, Supporting Information). The minor impurity peak at ≈1.20 ppm (marked as "Δ") in Figure 3c should be attributed to another decomposition product of Pyr-TEMPO, likely because of the breaking of nitroxyl radicals from N–O• to N–H. **Figure 4**d shows the CV curves of Pyr-TEMPO at pristine state and after galvanostatic cycling, respectively. The irreversible reduction peaks at −0.53 and −0.64 V versus SHE, respectively were assigned to the irreversible hydrogenation of Pyr-TEMPO to H-Pyr-TEMPO, as illustrated in the inset of Figure 3d. Moreover, an irreversible oxidation peak at 0.84 V was observed in the CV curve of [PyrPV]Cl_4 anolyte after cycling (Figure 3e), confirming the crossover of Pyr-TEMPO species. Clearly, these spectroscopic and CV results verify that the decomposition occurred not on the alkyl pyrrolidinium group in Pyr-TEMPO, but on the nitroxyl radical redox center of TEMPO species. In this way, our work provides straightforward proofs to clarify the capacity degradation mechanism of TEMPO/viologen AORFB systems based on a series of comprehensive characterizations.

To further investigate the redox mechanism and electrochemical behaviors of Pyr-TEMPO catholyte during cycling, the No-D ^1H and ^{13}C NMR spectroscopies were carried out to monitor the concentration variation of free radicals (Figure 4). This is because the No-D NMR spectra were not contaminated by the deuterated solvent, and thus could reflect the intrinsic signals of Pyr-TEMPO.[40] In the No-D ^1H NMR spectra of Pyr-TEMPO at pristine state (Figure 4a), the peaks of the alkyl pyrrolidinium group (marked as "1" to "6") broaden, owing to the presence of nitroxyl radicals.[41] The peaks of the TEMPO unit are not appeared except that the four broad methyl peaks (marked as "7") are visible. To guarantee a fully charged state, the AORFB was charged to 1.9 V and then maintained at 1.9 V for 5 min. Upon charging, the peaks of the alkyl pyrrolidinium group in Pyr-TEMPO sharpen and move towards lower chemical shifts. Then, upon discharging, the peaks of alkyl pyrrolidinium in Pyr-TEMPO broaden and move back towards higher chemical shifts. For example, after being charged to 1.90 V in the first cycle, the peak of methyl group on the pyrrolidinium (marked as "4′" at the charged state) sharpens and moves towards a lower chemical shift, from 3.69 to 2.89 ppm ($\Delta\delta = -0.80$ ppm), indicating the consumption of nitroxyl radicals upon charging; then, after discharged to 0.8 V in the first cycle, the peak of methyl group on the pyrrolidinium (marked as "4" in the pristine or discharged state) broadens and moves back towards a higher chemical shift, from 2.89 to 3.68 ppm ($\Delta\delta = 0.79$ ppm), indicating the regeneration of the nitroxyl radicals upon discharging. The shifts in the water solvent

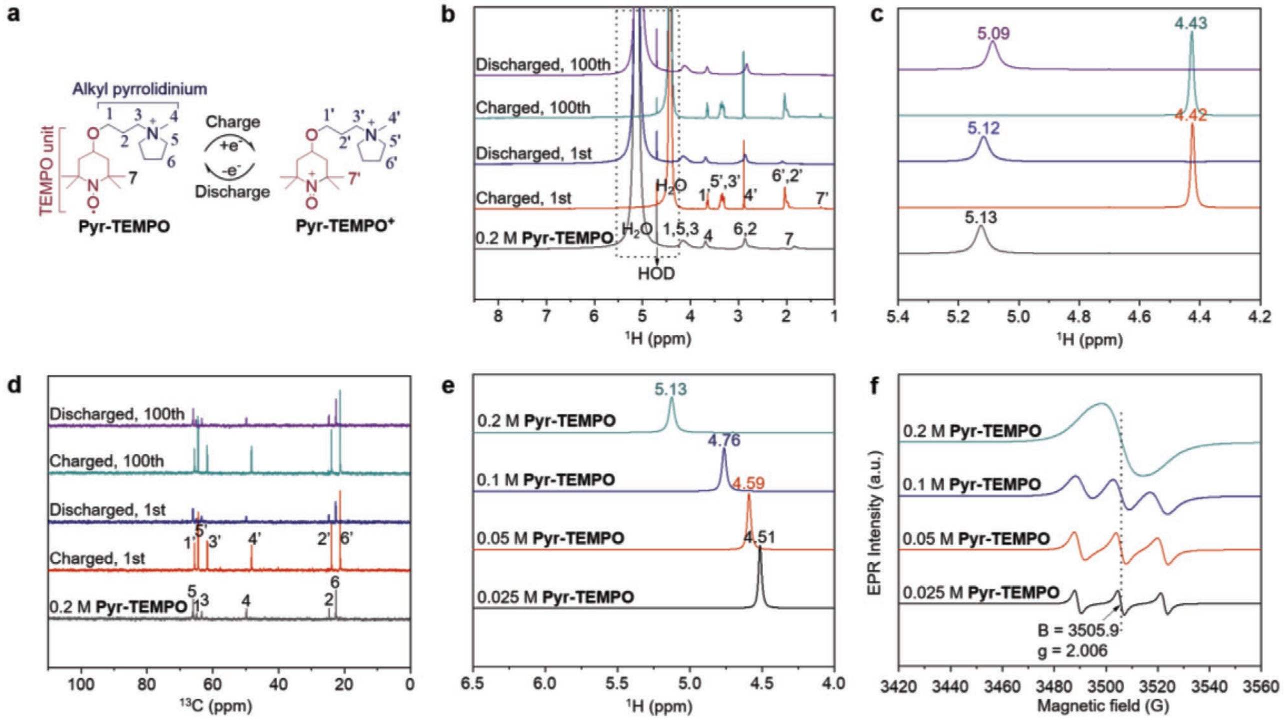

Figure 4. Redox mechanism studies of Pyr-TEMPO. a) Redox cycle of Pyr-TEMPO during charge and discharge processes. b) No-D ^1H NMR spectra of 0.2 м Pyr-TEMPO catholyte at pristine state, after fully charged and discharged in the first cycle and the 100th cycle, respectively. c) The water peak regions are magnified from the dashed box in (b). d) No-D ^{13}C NMR spectra of 0.2 м Pyr-TEMPO catholyte at pristine state, after fully charged and discharged in the first cycle and the 100th cycle, respectively. e) No-D ^1H NMR spectra showing the water peaks in Pyr-TEMPO catholytes with different concentrations (0.025–0.2 м). f) EPR spectra of Pyr-TEMPO catholyte with different concentrations (0.025–0.2 м).

resonance could reflect the change in the magnetic susceptibility of the solution. The water peaks in the No-D ^{1}H NMR spectra of Pyr-TEMPO catholyte show a similar variation trend to those of alkyl pyrrolidinium: upon charging, the water peak sharpens and moves towards a lower chemical shift, from 5.13 to 4.42 ppm ($\Delta\delta = -0.71$ ppm); upon discharging, the water peak broadens and moves towards a higher chemical shift, from 4.42 ppm to 5.12 ppm ($\Delta\delta = 0.70$ ppm). The peaks of alkyl pyrrolidinium and water shift back and forth (Figure 4b,c), indicating the reversible consumption and regeneration of the nitroxyl radicals upon charging and discharging. Notably, the water peak of 0.2 м Pyr-TEMPO catholyte at a fully charged state is at 4.42 ppm, and the value is identical to the water shift (4.42 ppm) in a simple 2.0 м NaCl aqueous solution as a control sample free of Pyr-TEMPO (Figure S16, Supporting Information). This indicates that most of the nitroxyl radicals have been consumed and the corresponding oxoammonium cations have formed. After 100 charge-discharge cycles, the peak shifts of water and alkyl pyrrolidinium almost recovered to the same positions as the 1st cycle, verifying the high redox reversibility of Pyr-TEMPO. In the No-D ^{13}C NMR spectra (Figure 4d), the carbon peaks of alkyl pyrrolidinium almost have a similar variation trend upon charging and discharging, expected that one carbon of alkyl pyrrolidinium (marked as “1” in the pristine or discharged state and as “1′” in the charged state), which is directly connected with the oxygen atom on the TEMPO unit, has an opposite variation of chemical shift. It is worthy to mention that the peak assignments of Pyr-TEMPO were further confirmed by a heteronuclear single quantum coherence (HSQC) NMR experiment (Figure S17, Supporting Information).

Furthermore, the No-D ^{1}H NMR spectra of Pyr-TEMPO catholytes with different concentrations (0.025–0.2 м) were analyzed (Figure 4e). The chemical shift of the water peak can reflect the concentration of radicals in the solution: when the radical concentration increases, the water peak moves towards a higher chemical shift; when the radical concentration decreases, the water peak moves towards a lower chemical shift. For example, when the concentration of Pyr-TEMPO increases from 0.025 to 0.2 м, the water peak remarkably shifts downfield, from 4.51 to 5.13 ppm, and such chemical shift variations are originated from the interaction between the nitroxyl radicals and water. As compared, the No-D ^{1}H NMR spectra of Pyr-TEMPO catholytes with different concentrations were also conducted after being charged to 1.90 V (Figure S18, Supporting Information), where the position of water peak almost had no shift, indicating that the interaction between water and radicals almost disappeared due to the formation of an oxoammonium cation (Pyr-TEMPO$^+$). In the EPR spectra of Pyr-TEMPO catholyte with different concentrations (Figure 4f), as the concentration increases from 0.025 to 0.2 м, the three lines gradually coalesce into a single broad line, which was typical of enhanced magnetic interactions such as exchange interaction of paramagnetic species.[42] The above NMR and EPR analyses reveal the interaction between the nitroxyl radicals with water. And this interaction may help to prevent the Pyr-TEMPO molecules from collision-caused structural decomposition, thus improving the cycling performance of Pyr-TEMPO/[PyrPV]Cl$_4$ AORFBs.

3. Conclusion

In summary, here we report the successful synthesis of TEMPO and extended viologen derivatives both functionalized by highly stable and hydrophilic alkyl pyrrolidinium groups with high solubility and an exceptionally large voltage gap. The two single-electron reductions of [PyrPV]Cl$_4$ were clearly verified by a simple electrochemical approach. The pyrrolidinium-functionalized Pyr-TEMPO displayed an extremely high solubility (>3.35 м in water), outstanding electrochemical reversibility, and fast electron transfer kinetics. The interaction between the nitroxyl radicals in Pyr-TEMPO and water molecule was verified, maybe helping to prevent the collision-caused side reactions and thus improving the cycling performance. As a result, the Pyr-TEMPO/[PyrPV]Cl$_4$ AORFB delivered excellent Coulombic efficiency, high energy efficiency, large power density, and durable cycling life. The crossover and decomposition of Pyr-TEMPO species were primarily responsible for the capacity degradation, which was comprehensively confirmed by the ^{1}H NMR, CV, and HRESIMS studies. Specifically, the Pyr-TEMPO species that crossed into the [PyrPV]Cl$_4$ anolyte would undergo irreversible hydrogenation on the nitroxyl radical redox center in the discharge process, and the decomposition of Pyr-TEMPO in the catholyte should be mostly due to the cleavage of nitroxyl radical from N–O• to N–H, thus leading to the capacity degradation. The crossover issue can be alleviated by introducing a positively charged group with a larger size or more positive charged groups into the TEMPO molecule, thus further improving the stability of AORFBs. This work presents effective electrochemical and spectroscopic approaches to clarify the redox behavior and capacity degradation mechanism of radical involved in AORFBs, providing an important foundation for the design of high-voltage, stable, and sustainable energy storage systems.

Supporting Information

Supporting Information is available from the Wiley Online Library or from the author.

Acknowledgements

The authors thank the funding supports from the National Key R&D Program of China (No. 2017YFA0208200), the National Natural Science Foundation of China (No. 22022505 and 21872069), the Fundamental Research Funds for the Central Universities (No. 0205-14380266), the Natural Science Foundation of Jiangsu Province (No. BK20200306 and BK20180008), and the 2021 Suzhou Gusu Leading Talents of Science and Technology Innovation and Entrepreneurship in Wujiang District.

Conflict of Interest

The authors declare no conflict of interest.

Data Availability Statement

The data that supports the findings of this study are available in the supplementary material of this article.

Keywords

AORFBs, high-voltage, organic radicals, pH-neutral, pyrrolidinium, redox-active materials

Received: November 7, 2021
Revised: January 22, 2022

[1] B. Dunn, H. Kamath, J.-M. Tarascon, *Science* **2011**, *334*, 928.
[2] M. Park, J. Ryu, W. Wang, J. Cho, *Nat. Rev. Mater.* **2017**, *2*, 16080.
[3] G. L. Soloveichik, *Chem. Rev.* **2015**, *115*, 11533.
[4] Z. Yang, J. Zhang, M. C. W. Kintner-Meyer, X. Lu, D. Choi, J. P. Lemmon, J. Liu, *Chem. Rev.* **2011**, *111*, 3577.
[5] H. Zhao, Q. Wu, S. Hu, H. Xu, C. N. Rasmussen, *Appl. Energy* **2015**, *137*, 545.
[6] Y. Yao, J. Lei, Y. Shi, F. Ai, Y.-C. Lu, *Nat. Energy* **2021**, *6*, 582.
[7] Y. Xu, Y. Wen, J. Cheng, Y. Yang, Z. Xie, G. Cao, *World Non-Grid-Connected Wind Power and Energy Conference (WNWEC 2009)*, IEEE, Nanjing, China **2009**, pp. 1–4.
[8] B. Yang, L. Hoober-Burkhardt, F. Wang, G. K. S. Prakash, S. R. Narayanan, *J. Electrochem. Soc.* **2014**, *161*, A1371.
[9] D. G. Kwabi, Y. Ji, M. J. Aziz, *Chem. Rev.* **2020**, *120*, 6467.
[10] T. Liu, X. Wei, Z. Nie, V. Sprenkle, W. Wang, *Adv. Energy Mater.* **2016**, *6*, 1501449.
[11] L. Liu, Y. Yao, Z. Wang, Y.-C. Lu, *Nano Energy* **2021**, *84*, 105897.
[12] R. Feng, X. Zhang, V. Murugesan, A. Hollas, Y. Chen, Y. Shao, E. Walter, N. P. N. Wellala, L. Yan, K. M. Rosso, W. Wang, *Science* **2021**, *372*, 836.
[13] J. Luo, B. Hu, M. Hu, Y. Zhao, T. L. Liu, *ACS Energy Lett.* **2019**, *4*, 2220.
[14] Y. Zhu, Y. Li, Y. Qian, L. Zhang, J. Ye, X. Zhang, Y. Zhao, *J. Power Sources* **2021**, *501*, 229984.
[15] D. G. Kwabi, K. Lin, Y. Ji, E. F. Kerr, M.-A. Goulet, D. D. Porcellinis, D. P. Tabor, D. A. Pollack, A. Aspuru-Guzik, R. G. Gordon, M. J. Aziz, *Joule* **2018**, *2*, 1894.
[16] C. Wang, X. Li, B. Yu, Y. Wang, Z. Wang, H. Wang, H. Lin, J. Ma, G. Li, Z. Jin, *ACS Energy Lett.* **2020**, *5*, 411.
[17] Q. Chen, Y. Lv, Z. Yuan, X. Li, G. Yu, Z. Yang, T. Xu, *Adv. Funct. Mater.* **2021**, 2108777.
[18] S. Pang, X. Wang, P. Wang, Y. Ji, *Angew. Chem., Int. Ed.* **2021**, *60*, 5289.
[19] L. Zhang, Y. Qian, R. Feng, Y. Ding, X. Zu, C. Zhang, X. Guo, W. Wang, G. Yu, *Nat. Commun.* **2020**, *11*, 3843.
[20] T. Janoschka, N. Martin, M. D. Hager, U. S. Schubert, *Angew. Chem., Int. Ed.* **2016**, *55*, 14427.
[21] S. Jin, E. M. Fell, L. Vina-Lopez, Y. Jing, P. W. Michalak, R. G. Gordon, M. J. Aziz, *Adv. Energy Mater.* **2020**, *10*, 2000100.
[22] J. Luo, B. Hu, C. Debruler, T. L. Liu, *Angew. Chem., Int. Ed.* **2018**, *57*, 231.
[23] Y. Liu, M.-A. Goulet, L. Tong, Y. Liu, Y. Ji, L. Wu, R. G. Gordon, M. J. Aziz, Z. Yang, T. Xu, *Chem* **2019**, *5*, 1861.
[24] B. Hu, C. Debruler, Z. Rhodes, T. L. Liu, *J. Am. Chem. Soc.* **2017**, *139*, 1207.
[25] B. Hu, Y. Tang, J. Luo, G. Grove, Y. Guo, T. L. Liu, *Chem. Commun.* **2018**, *54*, 6871.
[26] C. DeBruler, B. Hu, J. Moss, X. Liu, J. Luo, Y. Sun, T. L. Liu, *Chem* **2017**, *3*, 961.
[27] B. Hu, J. Luo, M. Hu, B. Yuan, T. L. Liu, *Angew Chem., Int. Ed.* **2019**, *58*, 16629.
[28] S. Jin, Y. Jing, D. G. Kwabi, Y. Ji, L. Tong, D. D. Porcellinis, M.-A. Goulet, D. A. Pollack, R. G. Gordon, M. J. Aziz, *ACS Energy Lett.* **2019**, *4*, 1342.
[29] T. Janoschka, N. Martin, U. Martin, C. Friebe, S. Morgenstern, H. Hiller, M. D. Hager, U. S. Schubert, *Nature* **2015**, *527*, 78.
[30] G. S. Nambafu, K. Siddharth, C. Zhang, T. Zhao, Q. Chen, K. Amine, M. Shao, *Nano Energy* **2021**, *89*, 106422.
[31] J. Winsberg, C. Stolze, A. Schwenke, S. Muench, M. D. Hager, U. S. Schubert, *ACS Energy Lett.* **2017**, *2*, 411.
[32] Z. Chang, D. Henkensmeier, R. Chen, *ChemSusChem* **2017**, *10*, 3193.
[33] D. R. MacFarlane, N. Tachikawa, M. Forsyth, J. M. Pringle, P. C. Howlett, G. D. Elliott, J. H. Davis, M. Watanabe, P. Simon, C. A. Angell, *Energy Environ. Sci.* **2014**, *7*, 232.
[34] M. Pan, J. Zou, R. Laine, D. Khan, R. Guo, X. Zeng, W. Ding, *J. Mater. Chem. A* **2019**, *7*, 18880.
[35] H. Neugebauer, F. Bohle, M. Bursch, A. Hansen, S. Grimme, *J. Phys. Chem. A* **2020**, *124*, 7166.
[36] O. Hammerich, B. Speiser, *Organic Electrochemistry*, CRC Press, Boca Raton **2016**.
[37] M. Pan, Y. Lu, S. Lu, B. Yu, J. Wei, Y. Liu, Z. Jin, *ACS Appl. Mater. Interfaces* **2021**, *13*, 44174.
[38] S. Hu, T. Li, M. Huang, J. Huang, W. Li, L. Wang, Z. Chen, Z. Fu, X. Li, Z. Liang, *Adv. Mater.* **2021**, *33*, 2005839.
[39] H. Wang, S. Y. Sayed, E. J. Luber, B. C. Olsen, S. M. Shirurkar, S. Venkatakrishnan, U. M. Tefashe, A. K. Farquhar, E. S. Smotkin, R. L. McCreery, J. M. Buriak, *ACS Nano* **2020**, *14*, 2575.
[40] M. Pan, N. Cao, W. Lin, X. Luo, K. Chen, S. Che, H. Li, C. Wang, *ChemSusChem* **2016**, *9*, 2351.
[41] E. W. Zhao, T. Liu, E. Jónsson, J. Lee, I. Temprano, R. B. Jethwa, A. Wang, H. Smith, J. Carretero-González, Q. Song, C. P. Grey, *Nature* **2020**, *579*, 224.
[42] Z. Huang, C. W. M. Kay, B. Kuttich, D. Rauber, T. Kraus, H. Li, S. Kim, R. Chen, *Nano Energy* **2020**, *69*, 104464.